Quantum Cascade Photonic-Crystal Microlasers

Raffaele Colombelli, Kartik Srinivasan, Mariano Troccoli, Oskar J. Painter, Claire F. Gmachl, et al.

Raffaele Colombelli, Kartik Srinivasan, Mariano Troccoli, Oskar J. Painter, Claire F. Gmachl, Donald M Tennant, A. Michael Sergent, Deborah L Sivco, Alfred Y Cho, Federico Capasso, "Quantum Cascade Photonic-Crystal Microlasers," Proc. SPIE 5365, Novel In-Plane Semiconductor Lasers III, (11 May 2004); doi: 10.1117/12.532586

SPIE.

Event: Integrated Optoelectronic Devices 2004, 2004, San Jose, CA, United States

Quantum Cascade Photonic-Crystal Microlasers

Raffaele Colombelli[1,5], Kartik Srinivasan[2], Mariano Troccoli[3], Oskar Painter[2], Claire F. Gmachl[1,6], Donald M. Tennant[1,4], A. Michael Sergent[1], Deborah L. Sivco[1], Alfred Y. Cho[1], and Federico Capasso[3]

[1] Bell Laboratories, Lucent Technologies, Murray Hill, NJ 07974, USA
[2] Applied Physics Department, California Institute of Technology, Pasadena, CA 91125, USA
[3] DEAS, Harvard University, Cambridge, MA 02138, USA
[4] New Jersey Nanotechnology Consortium, Murray Hill, NJ 07974, USA
[5] Institut d'Electronique Fondamentale, Universite Paris-Sud, 91405 Orsay, FRANCE
[6] Department of Electrical Engineering, Princeton University, Princeton, NJ 08544, USA

ABSTRACT

We describe the realization of Quantum Cascade photonic-crystal microlasers. Photonic and electronic band-structure engineering are combined to create a novel Quantum Cascade microcavity laser source. A high-index contrast two-dimensional photonic crystal forms a micro-resonator that provides feedback for laser action and diffracts light vertically from the surface of the semiconductor chip. A top metallic contact is used to form both a conductive path for current injection as well as to provide vertical optical confinement to the active region through a bound surface plasmon state at the metal-semiconductor interface. The device is miniaturized compared to standard Quantum Cascade technology, and the emission properties can in principle be engineered by design of the photonic crystal lattice. The combination of size reduction, vertical emission, and lithographic tailorability of the emission properties enabled by the use of a high-index contrast photonic crystal resonant cavity makes possible a number of active sensing applications in the mid- and far-infrared. In addition, the use of electrical pumping in these devices opens up another dimension of control for fundamental studies of photonic crystal and surface plasmon structures in linear, non-linear, and near-field optics.

Keywords: quantum cascade lasers, photonic crystals, photonic band-gaps, microlasers, vertically emitting lasers

1. INTRODUCTION

Quantum Cascade (QC) lasers have, within the span of a few years, established themselves as the leading tunable coherent semiconductor source in the mid-infrared (mid-IR) and far-infrared (far-IR) ranges of the electromagnetic spectrum.[1–3] Their uniqueness stems from the use of an intraband optical transition: the device is unipolar, and light is emitted when the electrons undergo a quantum jump between quantized conduction band states, called subbands, of a suitably designed semiconductor multi-quantum-well structure. However, due to the naturally transverse magnetic (TM) polarization of the intersubband transitions, QC lasers are intrinsically only in-plane emitters, with the electric-field vector perpendicular to the plane of the semiconductor layers. Surface emission cannot be easily achieved, although such a characteristic would be extremely desirable for several applications.

This work describes the development of a novel micro-resonator for QC lasers,[4] providing in-plane feedback and vertical extraction of the laser light through the use of a deeply etched two-dimensional (2D) photonic crystal (PC) structure.[5] The immediate advantage of this technology is the ability to design surface-emitting QC lasers, but the potential impact is much broader. Previous attempts to develop vertically emitting QC lasers made use of second-order Bragg gratings superimposed on conventional edge-emitting QC lasers,[6–8] but those works did not address the large size of the devices. The dimensions of the microlasers described here are greatly scaled down in comparison with standard QC technology, thus opening the way for the miniaturization and on-chip

Further author information: (Send correspondence to R.C. - E-mail: colombel@ief.u-psud.fr)

Novel In-Plane Semiconductor Lasers III, edited by Claire F. Gmachl, David P. Bour,
Proceedings of SPIE Vol. 5365 (SPIE, Bellingham, WA, 2004) · 0277-786X/04/$15 · doi: 10.1117/12.532586

integration of QC lasers for applications involving the use of multi-wavelength 2D laser arrays for spectroscopy, gas-sensing and imaging.[4]

PC-based QC lasers also represent an ideal system to perform fundamental research on photonic-bandgap structures. Compared to interband lasers, the characteristic length scale of the PC QC pattern is significantly larger due to the longer emission wavelengths of QC lasers, allowing optical lithography to be used as an alternative to e-beam lithography for pattern definition. Furthermore, the smaller ratio between the scale of etch-induced surface roughness and the operating wavelength can significantly reduce optical scattering. Leakage currents due to surface recombination, which are usually substantially increased by the etching of the PC pattern into the semiconductor material, are not present in QC lasers because of their unipolar nature. This is very much in contrast with diode lasers, where surface recombination is a serious obstacle to their use in conjunction with PC technology. Furthermore, the majority of PC *micro-resonator* laser work thus far has used optical pumping of undercut membrane geometries.[9] The demonstration of an electrically pumped, small-area PC laser in a non-undercut waveguide geometry is an important step in the development of PC microcavity lasers for practical applications.[4]

2. DESIGN

Photonic crystals are materials with a spatially periodic modulation of the dielectric constant, which can create a range of forbidden frequencies (band-gap) and dramatically alter the photonic density of states. A PC therefore affects the properties of photons in a manner analogous to the way that semiconductor crystals affect the properties of electrons.[10,11] Planar PC devices, employing a 2D photonic lattice with a conventional slab vertical waveguide, have been a particularly appealing device architecture due to the maturity of planar fabrication methods.[12] Two-dimensional PC slab waveguide lasers, which have typically operated at near-infrared (near-IR) wavelengths ($\lambda \approx$ 800-1700 nm), can be divided in two families: defect mode lasers and band-edge mode lasers. The former operate at frequencies inside the band-gap by incorporating an intentionally introduced defect in the lattice that supports resonator modes with high spatial localization.[9] Band-edge mode lasers, instead, operate in regions of energy-momentum space that have a very high photonic density of states, and corresponding small group velocity, as a result of the 2D distributed feedback of the photonic lattice.[13] To date, defect mode lasers with cavity dimensions at the wavelength scale have been demonstrated in an *optically-pumped* configuration only, with the PC holes completely etched through a waveguiding core layer that is usually a thin, free-standing membrane.[9,14] On the other hand, band-edge lasers typically have been reported as broad-area devices involving several hundred PC periods. These broad-area devices use a relatively shallow etch (weak grating) in a non-membrane geometry which is pumped either optically or electrically.[6–8,13,15,16]

In this work we consider the formation of a PC QC "microcavity band-edge laser", where an etch that penetrates through the laser active region and deep into the bottom waveguide cladding is employed. The deep etch produces (ideally) the same two-dimensional photonic crystal air-hole pattern in the lower refractive index bottom semiconductor cladding as in the top active region waveguide core, thus allowing for efficient vertical optical confinement of the guided mode.[17] This design reduces the diffraction of radiation into the substrate (enhancing the vertical extraction efficiency) and keeps the optical losses associated with free carrier absorption in the substrate to a minimum, while providing a high-index contrast semiconductor-air 2D grating for strong in-plane feedback. As a result, the band-edge devices studied in this work utilize only ten periods of the photonic lattice (less than 8 wavelengths in diameter), and are in fact effectively no larger in size than resonant cavities with a central defect region in the lattice, hence their definition as microcavity lasers (microlasers).

As a starting point for analysis of these planar photonic crystal structures, one may approximately treat the system as two-dimensional by incorporating an effective refractive index for the dielectric material, chosen to equal the effective index of the fundamental vertical waveguide mode.[18] The 2D photonic crystal in this work consists of an etched array of air holes arranged in a hexagonal (trigonal) array. This lattice was chosen not for the frequency band-gaps it forms (in two-dimensions this lattice does not have a frequency band-gap for TM polarized light), but rather because of its connected nature, necessary for efficient electrical injection. Note that the absence of a full 2D band-gap does not imply that strongly dispersive flat-bands cannot be formed for creating low-loss band-edge states, or that highly localized defect states cannot be formed.[19] The main criterion is that the photonic lattice provides high-index contrast so that strong optical feedback can be obtained over

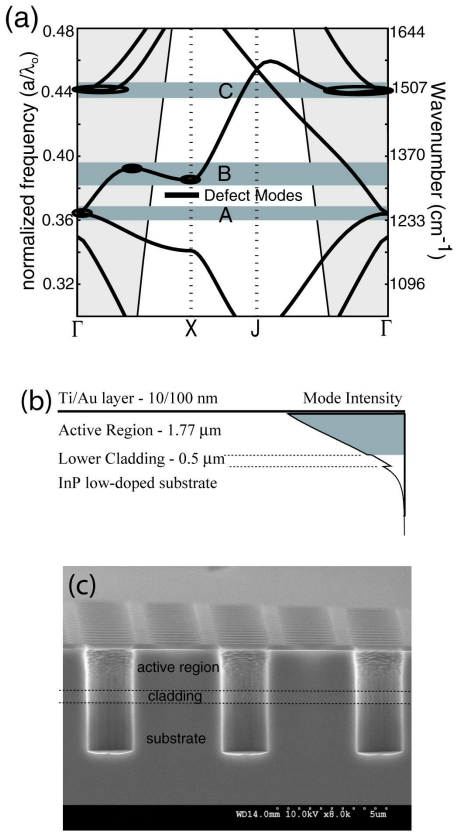

Figure 1. (a) Calculated two-dimensional in-plane TM bandstructure for a hexagonal lattice of air holes ($r/a = 0.30$, $n_{eff} = 3.345$). The flat band regions near the second order diffraction condition, labeled A, B, and C, are indicated by dark grey bands. For the devices with a central defect, the energy position of the highly localized defect modes is indicated by the thick short line between frequency regions A and B. (b) Layer structure of the device and intensity profile of the surface plasmon mode. The thicknesses of the surface-plasmon layer, the active region and the lower cladding are also shown. The detailed layer structure of the active region is described in Ref.[21] (c) Cross-section SEM of a portion of a PC QC device, showing the high surface quality of the etched holes and their depth (~ 4.8 μm). The etch depth has been chosen such that it penetrates well into the bottom cladding and substrate, in order to completely overlap with the mode in the vertical direction. The interfaces between the active region, cladding layer, and InP substrate are marked with dotted lines.

several lattice periods, setting the scale of the PC laser devices. The calculation of the in-plane band-structure for TM-polarized light, shown in Fig. 1(a), was performed using the plane wave expansion method[20] with an effective index of $n_{eff} = 3.35$ to account for the optical confinement normal to the plane of the semiconductor surface and with hole radius (r) to lattice spacing (a) ratio of $r/a = 0.30$.

In the bandstructure of Fig. 1(a) only the frequencies around the bands formed due to second-order Bragg diffraction are shown. Due to the mixing of forward and backward propagating plane-waves near the second-order Bragg condition (and other high-symmetry points of the reciprocal lattice), the group velocity of light slows down resulting in flat regions of dispersion. In these flat-band regions, low-loss resonant modes can be localized in *finite* lattice structures (such as the cavities described below) due to the reduction in group velocity over an extended region of wavevector space. Of particular importance to this work are the three frequency regions shown in Fig. 1(a) (highlighted in dark grey and labeled A, B, and C) which surround the flat-band regions in the frequency range close to the second-order Bragg condition. To place these band-edge resonances within the gain spectrum of the QC active material ($\lambda \sim 8$ μm), the approximate 2D analysis of Fig. 1(a) indicates that the lattice spacing should be chosen between $a = 2.85 - 3.6$ μm for a hexagonal lattice with $r/a = 0.30$.

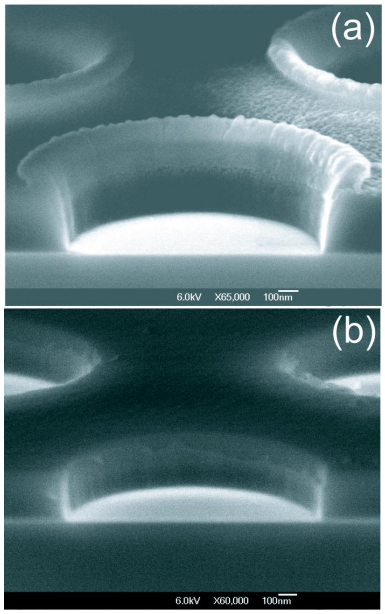

Figure 2. (a) SEM image of a semiconductor sample before the cleaning procedure: the polymeric buildup occurs during the hard mask etching. (b) SEM image of semiconductor sample after the cleaning procedure.

Vertical waveguiding in the third direction, normal to the semiconductor surface, is determined by the semiconductor and metal layers making up the QC laser structure as depicted in Fig. 1(b). This waveguiding, which has been treated up to this point simply through an effective waveguide index, reduces the symmetry of the system resulting in mixing of TE- and TM-polarizations, and opens up other radiative channels, either downwards into the substrate or vertically into the surrounding air. The QC heterostructure active region in the devices studied here is based on a 3-well vertical transition design (with emission wavelength $\lambda \approx 8$ μm) of the active region,[21] and it is grown by molecular beam epitaxy (MBE) on a low-doped InP substrate. A key element of the laser design is the use of a surface-plasmon waveguide to achieve vertical optical confinement (Fig. 1(b)).[22–24] This type of waveguide exhibits a maximum of the electric field intensity at the top semiconductor-metal interface, and results in a predominantly TM-polarized guided mode. Of particular relevance to this work is also the moderate thickness of the epitaxial material (≈ 2.4 μm compared to ≈ 5.2 μm for a standard dielectric waveguide) and the absence of AlInAs claddings in the surface plasmon waveguides. Both these characteristics dramatically ease the etching process (Fig. 1(c)), which - as described in Ref.[17] - must penetrate well into the bottom InP cladding to suppress radiation into the substrate.

3. FABRICATION

After a hard mask layer of silicon dioxide (SiO_2) 500 nm thick was deposited by plasma-enhanced chemical vapor-deposition, the PC pattern was written using electron beam lithography on a JEOL 9300FS 100kV system. We used a commercially available environmentally stabilized chemically amplified photo-resist (ESCAP), UV113. The chemically amplified resist was chosen because it features a good resolution and etching resistance, and it also requires a significantly lower dose than conventional single component resists. This allowed us to better populate our samples with practical writing times, an important requirement in view of the realization of 2D arrays of PC QC lasers with hundreds of micro-devices on a single semiconductor chip. The patterned e-beam resist was transferred to the underlying silicon dioxide hard mask layer via reactive ion etching using CHF_3, typically a 20 to 40 minute etch. The remaining resist was then solvent removed.

The choice of SiO_2 as a hard mask instead of Si_xN_y was dictated by the much steeper sidewall angle achievable with silicon dioxide. It proved critical to clean the polymeric buildup which occurs during the hard mask etching

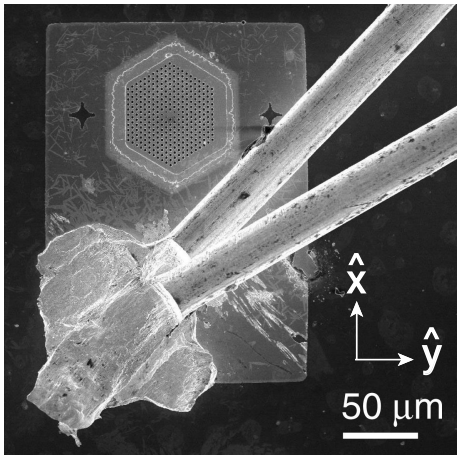

Figure 3. SEM image of a complete, wire-bonded laser device. The central patterned region sits in a hexagonal opening in the rectangular metal contact pad. The pad size is 210×150 μm. The PC cavity region is roughly 60 μm in diameter.

step (Fig. 2) in order to obtain a high quality transfer of the PC pattern into the active semiconductor layers. Fig. 2(a) shows that a thin layer of polymer tends to cover the whole sample, and its accumulation is particularly massive at the periphery of the holes in the insulator. Fig. 2(b) shows the patterned hard mask after the removal of the build up.

The transfer of the PC pattern to the semiconductor material (Fig. 1(c)) was achieved using an Oxford Instruments Plasma Technology inductively-coupled plasma reactive ion etch (ICP/RIE). The three primary requirements on the etch were (1) the etched holes need to extend through the core region significantly (2-3 μm) into the lower cladding, in order to minimize substrate radiation losses, (2) the etched holes need to be vertical to reduce loss and avoid an electrical short between the top contact and substrate, and (3) the etched sidewalls should be as smooth as possible to reduce losses (in addition to scattering losses, significant erosion of the core layer can reduce its effective index and potentially increase the vertical radiation losses).

The Cl_2-based plasma etch that we employed uses the high-density plasma produced by the ICP system to provide local surface heating of the sample and an increased efficiency in the sputter desorption of the $InCl_x$ products.[25] The ICP-RIE etch was studied as a function of ICP power (300-500 W) and RF power (100-350 W), with the chamber pressure (P=3 mTorr), no He backside cooling, and an Ar:Cl_2 gas chemistry kept fixed. The final ICP and RF powers chosen were 350 W and 250 W, respectively, and produced vertical sidewalls with an acceptable amount of sidewall roughness (Fig. 1(c)). Lower RF powers produced extremely pitted (and slightly angled) sidewalls throughout both the core and cladding layers (which we attribute to the decreased volatility of the $InCl_x$ etch products, resulting from the lower sample temperature and/or lower desorption rate caused by the reduced RF power), while higher RF powers created smooth sidewalls in the lower cladding and InP layers but increased roughness in the core layer (attributed to pitting that occurs in Al-containing layers that are etched at too hot a temperature). These results suggest that the sample temperature (generated by the plasma) is a leading factor affecting sidewall roughness. For our typical etch times (t $\approx$ 5 minutes), etch depths of 5 μm are achieved. Using the plasma as a mean of increasing the sample temperature indicates that the etch rate (and therefore the etch depth) will be a nonlinear function of time, as some amount of time is required for the temperature to equilibrate at a value hot enough for the $InCl_x$ compounds to be sufficiently volatile. This has been observed experimentally as etch times under 3 minutes have produced devices with angled holes and non-volatile $InCl_x$ etch products. Our etch creates a nearly 90° sidewall angle but suffers from roughness in the core layer. We believe that this is the result of the elevated sample temperature created by the high density plasma, which probably causes pitting of Al-containing layers.

The final step of the device fabrication consists in the application of electrical contacts, necessary to pump current through the system (see Fig. 3 for an SEM image of a complete device). It is important to emphasize that

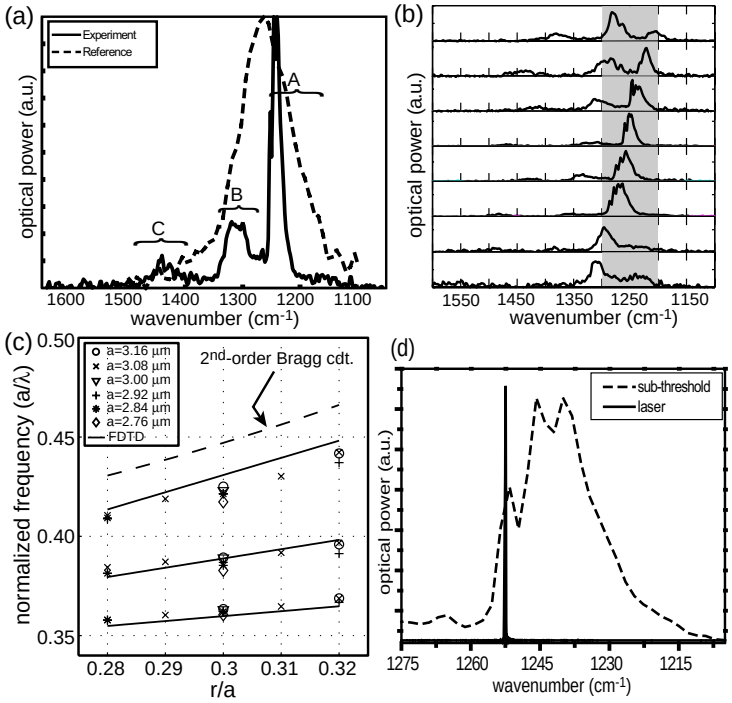

Figure 4. (a) Low-temperature EL (I = 700 mA, 50 ns pulse width, 84 kHz repetition rate) for a device with lattice spacing $a = 2.92$ μm and radius to lattice spacing ratio $r/a = 0.30$ (black continuous line). The reference spectrum (black dashed line) was collected from a device with $a = 2.69$ μm and $r/a = 0.28$ For this device the PC is not in resonance with the material gain peak: only the background intersubband EL spectrum is measured. The spectra were acquired in step-scan mode and with a spectral resolution of 4 cm^{-1} using a Nicolet Fourier transform infrared spectrometer (FTIR) and a nitrogen-cooled HgCdTe detector. (b) Emission spectra from a series of devices with different a and r/a. The grey shaded area corresponds to the FWHM of the QC gain spectrum . The instrument resolution was set to 0.125 cm^{-1}. (c) Tuning of the A, B, and C emission peaks as a function of r/a for a series of devices with different lattice spacings a, all plotted in normalized frequency units. The solid lines represent fits to FDTD simulations of the same devices. The dashed line represents the tuning of the second-order Bragg condition using an average refractive index given by the filling fraction of the lattice. (d) Close-up of the A emission peak for applied currents below (dashed line) and above (continuous line) laser threshold. The sub-threshold spectrum reveals that the peak is actually composed of 3 narrower resonances. The laser line always starts from the highest wavenumber resonance line within the A-peak. The laser emission was measured with the instrument resolution set to 0.125 cm^{-1}.

unipolar devices are not affected by leakage currents due to surface recombination, which are usually substantially increased (for interband lasers) by the etching of the PC pattern into the semiconductor material. The essential requirements we need to satisfy in order to fabricate a functional device are the localization of current injection into the PC QC devices, and the absence of metal deposition onto the holes sidewalls (to reduce losses and avoid device shorting from the top contact to the substrate). An insulating layer of silicon nitride was deposited on the sample. Hexagonal windows were opened in the insulator at the PC device sites via reactive ion etching. In the absence of a mesa, only the openings in the insulator silicon nitride pattern therefore define the regions of current injection.

A thick, low resistance Ti/Au (30/300 nm) contact was patterned up to the border of the hexagonal device, followed by the cleaning procedure. After the sample was thinned with an alumina polish from the back side, a metal back-contact was e-beam evaporated. As a last step, a vertical evaporation of thin Ti/Au (10/100 nm) was performed again on the top surface of the devices, to provide the surface-plasmon-carrying metal layer. The stringent requirement for vertical sidewalls in the active semiconductor etch is now evident, since this latter metal deposition must provide the topside electrical contact while preventing shorting of the same contact to the

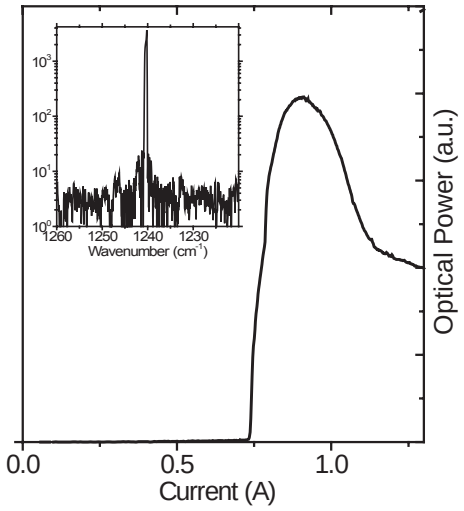

Figure 5. L-I characteristic for a typical device at 10 K. The lasers were operated in pulsed mode with 50 ns pulse width at 5 kHz repetition rate. The peak power for the devices with a central defect is in the range 400 μW to 1 mW. The devices without a central defect were significantly less powerful at similar current injection levels. Inset: Typical laser spectrum in log-lin scale: the device operates in single mode with a sidemode suppression of at least 20 dB. Some device showed the presence of a second, lower frequency mode, corresponding to the third resonance within the A emission peak

substrate. Metal is thus deposited between the holes and on the bottom of the holes,but only a limited amount of Ti/Au is deposited on the sidewalls.[26]

4. MEASUREMENTS

Two-dimensional arrays of devices were fabricated in which a and r of the hexagonal lattice were systematically varied from device-to-device within the array (a was varied between 2.69 μm and 3.00 μm along one axis of the array; r/a was varied between 0.28 and 0.32 along the other axis). In addition, two types of cavities were fabricated for each lattice spacing and hole radius in the array: one with a central defect, and another one with no central defect (a control sample). Electroluminescence (EL) measurements were performed at a temperature of 10 K and light was collected vertically from the top surface of the devices.

Fig. 4(a) (black dashed line) shows that when the PC modes are not in resonance with the gain spectrum peak (for detuned hole radius or lattice spacing), the emission has a near-Lorentzian shape with a full-width at half-maximum (FWHM) of ~ 100 cm^{-1} centered at the design wavelength of the QC heterostructure. For values of a and r where the PC modes overlap with the gain spectrum peak, a set of three emission peaks (which we label A, B, and C in correspondence with the frequency regions of the band structure in Fig. 1(a)), emerge on top of the broad EL spectrum (Fig. 4(a), black continuous line). The spectral position of these peaks can be tuned as a function of lattice spacing and hole radius as shown in Fig. 4(b), demonstrating that they indeed are related to Bragg scattering in the PC microcavity. Additionally, little difference is seen in the emission spectra between the cavities with a central defect and those without a central defect (control sample), an indication that the emission peaks are not related to highly localized defect states.

To better understand the nature of these emission peaks, we performed 2D finite-difference time-domain (FDTD) simulations of the finite cavity structure (as in the measured devices) with ten periods of holes and a hexagonal boundary. The near-field profiles of modes from within each of the 3 sets of resonances confirm that their dominant Fourier components are consistent with the **k**-space positions of the flat band regions indicated in Fig. 1(a). The near-field profiles also show that the C-peak resonant modes display a strong field overlap with the air holes, while resonances from the A- and B-peaks have fields that are largely confined into the

semiconductor regions. As a result, we expect that peak C will tune more strongly as a function of the hole radius than either of peaks A or B. This is confirmed by both experimental and FDTD results as shown in Fig. 4(c). The positive identification of the highest wavenumber set of resonances as the C-peak provides a reference point from which the A- and B-peaks can then be identified.

Fig. 4(d) shows a close-up of the A emission peak for one of the lasing devices: it is actually composed of three narrower resonances. Such behavior is common to all the measured devices. With further increase in applied current, the devices with the A-peak resonances best aligned with the gain peak reach lasing threshold. No mesa was etched around the devices. The absence of a mesa was chosen to eliminate Fabry-Perot like resonances, but it also makes it difficult to give an accurate estimate of the local current density at threshold for laser action, since the actual area across which the injected current is spread is not known. Etching a mesa around the PC QC may reduce the observed threshold current, however for the initial demonstration the absence of a mesa was a key feature since it ruled out other feedback mechanisms for the laser and confirmed that the PC itself is acting as a microcavity. The majority of the PC QC devices exhibit single mode laser emission in pulsed mode, with a sidemode suppression ratio of at least 20 dB (Fig. 5, inset), and the output wavelength could also be tuned by selecting - *from the same semiconductor chip* - devices with different lattice spacings or hole radius(see Ref.[4]).

5. LASING MODE IDENTIFICATION

In order to identify the lasing mode, far-field emission and polarization measurements of the PC QC lasers were performed.[27] Figs. 6(a-b) show two typical far-field intensity patterns of the lasing mode from PC microcavities with and without a central defect region, respectively. In these measurements the far-field emission pattern normal to the surface of the semiconductor laser chip was mapped out by scanning a 300 μm $\times$ 300 μm nitrogen-cooled HgCdTe detector at a distance of approximately 10 cm without any intermediate optics. The average surface-normal far-field polarization of the lasing mode (Fig. 6(d)), measured by using a lens to focus the light on the HgCdTe detector with a polarizer placed in front of it, was found to be predominantly polarized along the $\hat{y}$-direction (cavity orientation as in Fig. 3). In addition, we studied the polarized spatial distribution of the vertically emitted field intensity by placing a polarizer in front of a micro-bolometer camera fitted with a lens. The polarized emission patterns for electric field polarization along the $\hat{x}$- and $\hat{y}$-axis are shown in Figures 6(e) and (f), respectively.

From the $\hat{x}$- and $\hat{y}$-polarized intensity patterns the symmetry of the lasing mode may be determined.[5, 28, 29] For example, the nodal lines (lines of near-zero intensity in the images) along the $\hat{x}$- and $\hat{y}$-axis of Fig. 6(f) for the $\hat{y}$-polarized intensity pattern are consistent exclusively with an electromagnetic field mode which is odd (parity -1) under a mirror symmetry about the $\hat{y}$-axis and which is even (parity +1) under a mirror symmetry about the $\hat{x}$-axis. In the mathematical notation of group theory, such a mode is said to have B_1 symmetry, where B_1 is the label of one of the irreducible representations (IRREPS) of the point group of a rectangle. A similar conclusion is reached by studying the $\hat{x}$-polarized intensity pattern of Fig. 6(e) which has anti-nodes on both the $\hat{x}$- and $\hat{y}$-axis. Thus, the two polarized intensity patterns of Figs. 6(e-f) indicate that the laser emission is single mode and that the laser mode is of B_1 symmetry.

To study the vertical emission characteristics of the modes of the PC microcavity, full three-dimensional (3D) FDTD simulations of the hexagonal symmetry non-defect cavity were performed. The etched hole depth was taken to be 5 microns and a 200 nm thick idealized "perfectly conducting" metal top contact was used to guide the TM surface wave (at a wavelength of ≈ 8 μm this is a good approximation for a Au metal contact[30, 31]). In order to reduce the size and time of the simulation, the cavity was limited to 6 periods of the hexagonal lattice (as opposed to the experimental 10 periods). Mirror boundary conditions were used to project the modes of the hexagonally symmetric cavity onto a basis compatible with the symmetry of a rectangle whose principal axes lie along the $\hat{x}$- and $\hat{y}$-axis of the PC microcavity.

The highest frequency resonant mode of the A-peak was found to be of B_1 symmetry (we refer to this mode simply as the B_1 mode from here on). This is consistent with the experimentally measured emission spectrum and with the laser near-field symmetry (Fig. 6(e-f)) as discussed above. Fig. 7 shows the $\hat{z}$-component (i.e. normal to the semiconductor-metal surface) of the electric field (E_z) for the B_1 mode. The values of the electric field have been sampled in the plane beneath the metal contact in the semiconductor active region. It is interesting

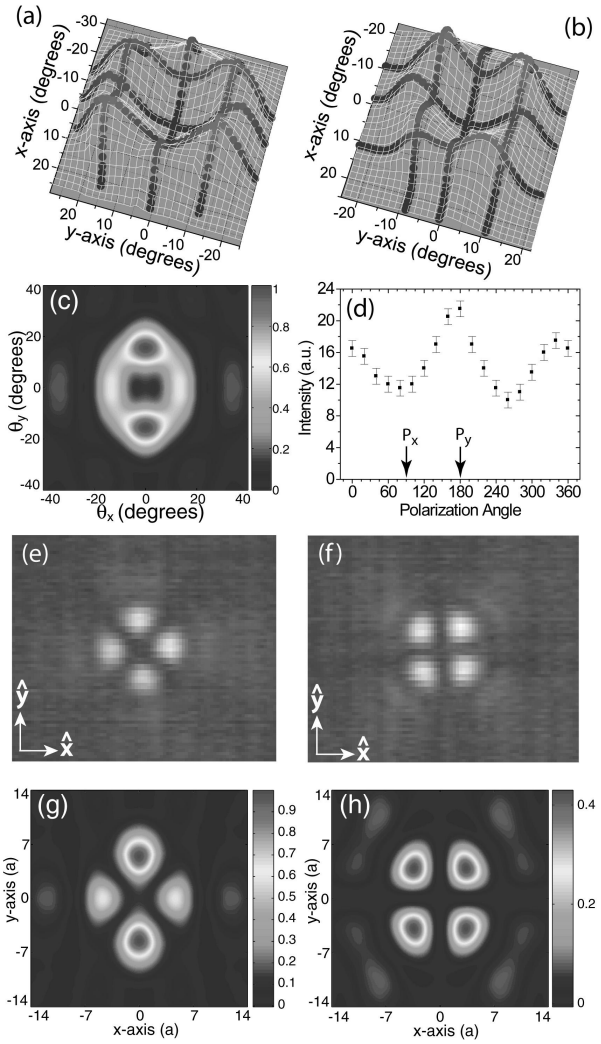

Figure 6. Far-field emission pattern of the PC microcavity lasers with (a) and without (b) central defect regions. The far-field pattern of a laser structure with a central defect region shows a slightly more elongated shape along the $\hat{y}$-axis of the PC cavity (the extended direction of the central defect region - cavity orientation as in Fig. 3). The measurements were performed by scanning a nitrogen-cooled HgCdTe detector in front of the laser device with no intermediate optics. The experimental data are shown as dots. An interpolation of the line scans (shown as a light grid) is used to generate an approximate 2D intensity image. (c) FDTD simulation of the far-field intensity pattern for the high-frequency mode within the A-peak set of resonances. (d) Polarization dependence of the laser emission in the far-field. (e) Polarized emission pattern (taken in a plane close to the near-field of the PC cavity surface) of a typical device for a polarization of the electric field along the $\hat{x}$-axis of the cavity. The measurement has been performed using a micro-bolometer mid-IR camera fitted with a lens. The device was operated above laser threshold in pulsed mode. (f) Polarized emission pattern for a polarization of the electric field along the $\hat{y}$-axis of the cavity and similar measurement conditions as in (e). FDTD calculated $\hat{x}$-polarized (g) and $\hat{y}$-polarized (h) vertical emission pattern at a few wavelengths above the surface of a non-defect PC cavity (see text for details).

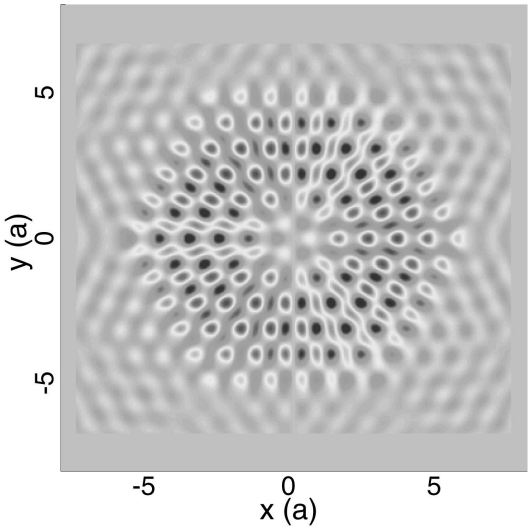

Figure 7. FDTD simulation of the high-frequency B_1 symmetry mode lying within the A-peak frequency range. Plot of E_z (electric field normal to the semiconductor surface) in the plane of the PC cavity just beneath the metal contact in the semiconductor active region.

to note, in hindsight, that this mode has only a small overlap with the central region of the PC cavity. This characteristic may partially explain the preferential selection of the B_1 mode as the lasing mode. Due to the expected in-plane spreading resistance in the etched PC region, the current injection (and consequently the gain) is most likely higher in the periphery of the PC. Furthermore, the B_1 mode's small overlap with the central region of the PC cavity is consistent with the similarity of the measured *frequencies* of the laser mode for both the defect and non-defect cavities. As a matter of fact, the entire electroluminescence spectra of both types of cavities are very similar. The noticeable absence - in cavities with a central defect- of the theoretically expected highly-localized defect mode resonances between the A- and B-peaks also lends support to the theory of higher current injection in the periphery of the PC.

Calculations of the vertically emitted radiation field, taken in a plane several wavelengths above the PC cavity surface, were performed by eliminating the non-propagating FDTD near-field components and introducing - to simulate the experimental conditions - a 30° collection angle cut-off for the imaging optics. The resulting $\hat{x}$- and $\hat{y}$- polarized intensity patterns of the B_1 mode are shown in Figs. 6(g-h), and are found to be in striking correspondence with the micro-bolometer camera measurements of Figs. 6(e-f). The theoretical far-field emission pattern was also calculated by transforming the FDTD generated radiation field into the far-field[32] and it is shown in Fig. 6(c). The increased intensity of the two lobes on the $\hat{y}$-axis in Fig. 6(g) of the $\hat{x}$-polarized intensity and in Fig. 6(c) of the far-field pattern are a result of inadvertent symmetry breaking of the hexagonal symmetry of the PC cavity due to discretization errors in employing the mirror boundary conditions in the FDTD simulation. In this case, the computed near-field under the metal contact is still very symmetric, as shown in Fig. 7(a). The symmetry breaking in the measured far-field (experimentally we observe the opposite effect, i.e. more intensity in the $\hat{y}$-polarization (Figs. 6(a,b,d)), is most likely a result of a similar subtle near-field effect due to the rectangular metal contact geometry.

The 3D FDTD calculated radiative quality-factor (Q) of the B_1 mode was found to be roughly a factor of two higher than the Q value of the neighboring A-peak resonant modes, helping explain why it is the first mode to lase. After calculating the in-plane, top (vertical), and bottom (substrate) radiation rates, as given by effective cavity quality-factors, we obtain an estimate for the vertical extraction efficiency of the PC microcavity laser. The estimation gives $\eta_v = Q_v^{-1}/(Q_{||}^{-1} + Q_v^{-1} + Q_s^{-1} + Q_a^{-1}) \approx 3\%$. The vertical extraction of light in this case is due to the fact that the resonances forming the A-peak sit near the Γ-point of the reciprocal lattice (Figs. 1(a)). They contain therefore small in-plane Fourier components which can radiate into the surrounding air, exactly as

in a second order distributed Bragg reflector. The coupling of radiation from the bottom semiconductor-metal interface to the top metal-air interface (from which the radiation finally escapes) is mediated through the air holes, as well as through the metal itself (although this effect has not been included in our calculations) due to the fact that the metal contact layer in the PC region is only 100 nm thick.

6. CONCLUSIONS

The QC photonic crystal microlasers described in this work bring together the advanced electronic band-gap engineering exploited in quantum cascade intersubband lasers and the optical dispersion engineering of photonic crystals. The result is a novel photonic crystal intersubband injection laser that opens new horizons in device design and applications in the mid- and far-infrared ranges of the electromagnetic spectrum.[4] The initial demonstration of a surface-emitting microcavity QC laser is but a first step. Further investigation of these types of lasers will initially focus on improved photon localization in highly localized defect states, a task that can be achieved by improving the electrical injection into the devices. Another immediate advantage of these novel devices is the possibility of engineering their far-field emission patterns through tailoring of the photonic lattice, or even of the contact pads themselves if the role of surface plasmons in affecting the near-field can be confirmed. The extension of this technology to the recently developed THz QC lasers may also be very attractive. Finally, the control afforded by the electrical injection of the PC QC lasers will also enable additional flexibility in the study of novel photonic crystal structures and of surface-plasmon mediated optical phenomena. Electrically beam steerable arrays can for instance be envisaged, as well as new lasers based on nonlinear photonic crystals, achieved for example by filling the holes with appropriate nonlinear materials.

ACKNOWLEDGMENTS

This work was partly supported by DARPA/ARO under contract number DAAD19-00-C-0096 and by the Charles Lee Powell Foundation. We acknowledge useful discussions and help from Axel Straub, Ken Steeples, Milton L. Peabody, Kirk Baldwin, Arthur Erbe, and Roberto Paiella. We thank Rainer Martini for lending us the micro-bolometer camera. K.S thanks the Hertz Foundation for its financial support.

REFERENCES

1. F. Capasso, R. Paiella, R. Martini, R. Colombelli, C. Gmachl, T. Myers, M. S. Taubman, R. M. Williams, C. G. Bethea, K. Unterrainer, H. Y. Hwang, D. L. Sivco, A. Y. Cho, H. Liu, and E. A. Whittaker, "Quantum Cascade Lasers: Ultrahigh-Speed Operation, Optical Wireless Communication, Narrow Linewidth, and Far-Infrared Emission," *IEEE J. Quantum Elect.* **38**, pp. 511–531, June 2002.
2. R. Kohler, A. Tredicucci, F. Beltram, H. Beere, E. Linfield, A. Davies, D. Ritchie, R. Iotti, and F. Rossi, "Terahertz semiconductor-heterostructure lasers," *Nature* **417**, pp. 156–159, May 2002.
3. M. Beck, D. Hofstetter, T. Aellen, J. Faist, U. Oesterle, M. Ilegems, E. Gini, and H. Melchior, "Continuous Wave Operation of a Mid-Infrared Semiconductor Laser at Room Temperature," *Science* **295**, pp. 301–305, Jan. 2002.
4. R. Colombelli, K. Srinivasan, M. Troccoli, O. Painter, C. Gmachl, D. M. Tennant, A. M. Sergent, D. L. Sivco, A. Y. Cho, and F. Capasso, "Quantum Cascade Surface-Emitting Photonic-Crystal Laser," *Science* **302**, pp. 1374–1377, Nov. 2003.
5. J. D. Joannopoulos, R. D. Meade, and J. N. Winn, *Photonic Crystals*, Princeton University Press, Princeton, New Jersey, 1995.
6. D. Hofstetter, J. Faist, M. Beck, and U. Oesterle, "Surface-emitting 10.1 μm quantum-cascade distributed feedback lasers," *Appl. Phys. Lett.* **75**, pp. 3769–3771, Dec. 1999.
7. W. Schrenk, N. Finger, S. Gianordoli, L. Hvozdara, G. Strasser, and E. Gornik, "Surface-emitting distributed feedback quantum-cascade lasers," *Appl. Phys. Lett.* **77**(14), pp. 2086–2088, 2000.
8. I. Vurgaftman and J. R. Meyer, "Design optimization for high-brightness surface-emitting photonic-crystal distributed-feedback lasers," *IEEE J. Quantum Elect.* **39**, pp. 689–700, June 2003.
9. O. Painter, R. K. Lee, A. Yariv, A. Scherer, J. D. O'Brien, P. D. Dapkus, and I. Kim, "Two-Dimensional Photonic Band-Gap Defect Mode Laser," *Science* **284**, pp. 1819–1824, June 1999.

10. E. Yablonovitch, "Inhibited Spontaneous Emission in Solid-State Physics and Electronics," *Phys. Rev. Lett.* **58**, pp. 2059–2062, May 1987.
11. J. D. Joannopoulos, P. R. Villeneuve, and S. H. Fan, "Photonic crystals: Putting a new twist on light," *Nature* **386**, pp. 143–149, Mar. 1997.
12. A. Scherer, J. L. Jewell, and J. P. Harbison, "Lasing in sub-micron wide vertical cavity microlasers," *Opt. Phot. News* **2**, p. 9, dec 1991.
13. M. Imada, S. Noda, A. Chutinan, T. Tokuda, M. Murata, and G. Sasaki, "Coherent two-dimensional lasing action in surface-emitting laser with triangular-lattice photonic crystal structure," *Appl. Phys. Lett.* **75**, pp. 316–318, July 1999.
14. H. Park, J. Hwang, J. Huh, H. Ryu, Y. Lee, and J. Hwang, "Nondegenerate monopole-mode two-dimensional photonic band gap laser," *Appl. Phys. Lett.* **79**, pp. 3032–3034, Nov. 2001.
15. M. Notomi, H. Suzuki, and T. Tamamura, "Directional lasing oscillation of two-dimensional organic photonic crystal lasers at several photonic band gaps," *Appl. Phys. Lett.* **78**, pp. 1325–1328, Mar. 2001.
16. H.-Y. Ryu, S.-H. Kim, Y.-J. Lee, Y.-H. Lee, and J.-S. Kim, "Very-low-threshold photonic band-edge lasers from free-standing triangular photonic crystal slabs," *Appl. Phys. Lett.* **80**, pp. 3476–3478, May 2002.
17. B. D'Urso, O. Painter, J. O'Brien, T. Tombrello, A. Scherer, and A. Yariv, "Modal reflectivity in finite-depth two-dimensional photonic-crystal microcavitites," *J. Opt. Soc. Am. B* **15**, pp. 1155–1159, Mar. 1998.
18. O. Painter, J. Vučković, and A. Scherer, "Defect Modes of a Two-Dimensional Photonic Crystal in an Optically Thin Dielectric Slab," *J. Opt. Soc. Am. B* **16**, pp. 275–285, Feb. 1999.
19. K. Srinivasan and O. Painter, "Momentum space design of high-Q photonic crystal optical cavities," *Opt. Express* **10**, pp. 670–684, July 2002.
20. K. Sakoda *J. Appl. Phys.* **84**, p. 1210, Mar. 1998.
21. C. Gmachl, A. Tredicucci, federico Capasso, A. L. Hutchison, D. L. . Sivco, J. N. Baillargeon, and A. Y. Cho, "High-power $\lambda \approx 8$ μm quantum cascade lasers with near optimum performance," *Appl. Phys. Lett.* **72**, pp. 3130–3132, June 1998.
22. C. Sirtori, C. Gmachl, F. Capasso, J. Faist, D. L. Sivco, A. L. Hutchinson, and A. Y. Cho, "Long-wavelength ($\lambda \approx 8 - 11.5$ micron) semiconductor lasers with waveguides based on surface plasmons," *Opt. Lett.* **23**, pp. 1366–1368, Sept. 1998.
23. A. Tredicucci, C. Gmachl, F. Capasso, A. L. Hutchinson, D. L. Sivco, and A. Y. Cho, "Single-mode surface-plasmon laser," *Appl. Phys. Lett.* **76**, pp. 2164–2166, Apr. 2000.
24. R. Colombelli, F. Capasso, C. Gmachl, A. L. Hutchinson, D. L. Sivco, A. Tredicucci, M. C. Wanke, and A. M. Sergent, "Far-infrared surface-plasmon quantum-cascade lasers at 21.5 μm and 24 μm wavelengths," *Appl. Phys. Lett.* **78**, pp. 2620–2622, Apr. 2001.
25. C. Youtsey and I. Adesida, *Handbook of Advance Plasma Processing Techniques*, Springer, Berlin, 2000.
26. R. Colombelli, K. Srinivasan, M. Troccoli, O. Painter, C. Gmachl, D. M. Tennant, A. M. Sergent, D. L. Sivco, A. Y. Cho, and F. Capasso, "Fabrication technologies for Quantum Cascade microlasers." manuscript in preparation, (2003).
27. K. Srinivasan, O. Painter, R. Colombelli, C. Gmachl, D. Sivco, A. Y. Cho., M. Troccoli, F. Cappaso, and A. Y. Cho, "Lasing mode pattern of a quantum cascade photonic crystal surface-emitting microcavity laser." manuscript in preparation, (2003).
28. M. Tinkham, *Group Theory and Quantum Mechanics*, International Series in Pure and Applied Physics, McGaw-Hill, Inc., New York, NY, 1964.
29. O. Painter and K. Srinivasan, "Localized defect states in two-dimensional photonic crystal slab waveguides: a simple model based upon symmetry analysis," *Phys. Rev. B* , May 2003.
30. L. Martin-Moreno, F. J. Garcia-Vidal, H. J. Lezec, K. M. Pellerin, T. Thio, J. B. Pendry, and T. W. Ebbeson, "Theory of Extraordinary Optical Transmission through Subwavelength Hole Arrays," *Phys. Rev. Lett.* **86**, pp. 1114–1117, Feb. 2001.
31. J. D. Jackson, *Classical Electrodynamics*, John Wiley & Sons, Inc., New York, NY, 2nd ed., 1975.
32. J. B. Judkins and R. W. Ziolkowski, "Finite-difference time-domain modeling of non-perfectly conducting metallic thin-film gratings," *J. Opt. Soc. Am. B* **12**, pp. 1974–1983, Sept. 1995.